PNAS RESEARCH ARTICLE | BIOPHYSICS AND COMPUTATIONAL BIOLOGY

Membrane localization accelerates association under conditions relevant to cellular signaling

William Y. C. Huang[a,1,2], Steven G. Boxer[b], and James E. Ferrell Jr.[a,c,1]

Edited by Michael Rosen, The University of Texas Southwestern Medical Center, Dallas, TX; received November 11, 2023; accepted January 16, 2024

Translocation of cytoplasmic molecules to the plasma membrane is commonplace in cell signaling. Membrane localization has been hypothesized to increase intermolecular association rates; however, it has also been argued that association should be faster in the cytosol because membrane diffusion is slow. Here, we directly compare an identical association reaction, the binding of complementary DNA strands, in solution and on supported membranes. The measured rate constants show that for a 10-μm-radius spherical cell, association is 22- to 33-fold faster at the membrane than in the cytoplasm. The kinetic advantage depends on cell size and is essentially negligible for typical ~1 μm prokaryotic cells. The rate enhancement is attributable to a combination of higher encounter rates in two dimensions and a higher reaction probability per encounter.

receptor signaling | membrane-associated proteins | Ras activation | bimolecular reaction | reduction of dimensionality

The translocation of signaling molecules from the cytosol to the cell membrane represents a key step in many signaling pathways (1). The process is exemplified by Ras activation in receptor tyrosine kinase (RTK) signaling (Fig. 1*A*) (2–4). Autophosphorylated transmembrane receptors recruit the nucleotide exchange factor Son of Sevenless (Sos) from the cytosol via one (Grb2) or two (Shc plus Grb2) adaptor proteins. Membrane-associated Sos then activates membrane-bound Ras, which in turn activates the MAP kinase (MAPK) cascade and initiates transcriptional programs for proliferation, differentiation, cell motility, and/or survival. Despite the fact that Sos activation is a complex, multistep process (5), the artificial recruitment of Sos to the membrane in the absence of receptor activation is sufficient to activate Ras, the MAPK pathway, and downstream transcriptional reporters (6, 7). Reconstitution of the Ras-Sos system shows that localizing the reaction to membranes substantially increases the turnover rate of nucleotide exchange (8, 9). Thus, membrane localization promotes greater signal output in this context. A wide variety of other signaling proteins also translocate to the membrane to become activated and/or to find targets, including phospholipase C gamma (PLCγ), phosphatidylinositol 3-kinase (PI3K), and both 3-phosphoinositide-dependent protein kinase 1 (PDK1) and its target Akt (10, 11). This last example is particularly striking: The activation of Akt depends upon the translocation of both its activator, PDK1, and Akt itself, to the plasma membrane. Thus, membrane translocation is a recurring theme in eukaryotic signaling.

This raises the fundamental question of how membrane localization promotes signaling. The potential advantages of a 2D search over a 3D search have long been of interest to theoreticians (12–19). For example, Pólya's theorem shows that random walks on a grid in 2D will always find a stationary target, but in 3D the probability is less than one (12). Adam and Delbrück further explored the question and showed that translocation of molecules from the cytoplasm to a cell membrane may increase first-encounter rates and association rates (13). This concept has been elaborated on in a large number of subsequent papers (1, 14–17, 19–22). In the framework of Michaelis–Menten kinetics, a faster association rate could directly speed the activation of the target if the process is diffusion-controlled, or increase the steady-state concentration of protein–target complexes and thereby increase the rate of target activation if the process is reaction-controlled.

However, membrane translocation would also be expected to slow diffusion because membranes are more viscous than cytoplasm. Whether or not this slowing would completely counteract the positive effects of membrane translocation is currently a matter of conjecture (Fig. 1*B*), with some estimating that a membrane-associated 2D search should be quicker than a cytoplasmic 3D search (13, 17, 19, 21), and others predicting the opposite (20, 23, 24). Furthermore, it is not clear to what extent the first encounter rate between two species determines the association rate (20, 22, 24).

Here, we set out to resolve these uncertainties through experiments comparing an identical association reaction in solution and at the membrane, a situation most closely analogous to the PDK1–Akt system. We chose a model system approach to enable

Significance

In eukaryotic cells, the translocation of signaling proteins from the cytosol to the cell membrane is a recurring theme in many signaling pathways. Why translocation occurs has been a subject of lively debate, with many theoretical propositions but little experimental evidence. One such hypothesis states that intermolecular encounters are more frequent on membranes than in solution. Although attractive, this idea has been challenged by the fact that membrane diffusion is significantly slower. In this study, we set out to answer this question by experimentally measuring the association rate of an identical reaction in solution and on membranes. The results confirm that association at the membrane is in fact faster, with additional mechanistic insights into the origins of the rate enhancement.

Author affiliations: [a]Department of Chemical and Systems Biology, Stanford University School of Medicine, Stanford, CA 94305; [b]Department of Chemistry, Stanford University, Stanford, CA 94305; and [c]Department of Biochemistry, Stanford University School of Medicine, Stanford, CA 94305

Author contributions: W.Y.C.H. and J.E.F. designed research; W.Y.C.H. performed research; W.Y.C.H., S.G.B., and J.E.F. analyzed data; S.G.B. edited/commented on the paper; and W.Y.C.H. and J.E.F. wrote the paper.

The authors declare no competing interest.

This article is a PNAS Direct Submission.

[1]To whom correspondence may be addressed. Email: whuang@jhu.edu or james.ferrell@stanford.edu.

[2]Present address: T. C. Jenkins Department of Biophysics, Johns Hopkins University, Baltimore, MD 21218.

This article contains supporting information online at https://www.pnas.org/lookup/suppl/doi:10.1073/pnas.2319491121/-/DCSupplemental.

Published March 1, 2024.

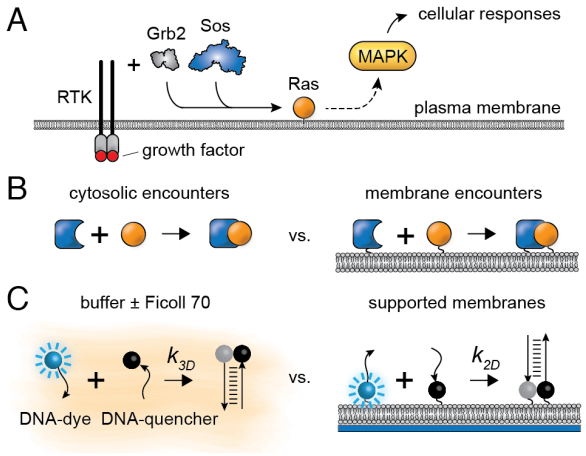

Fig. 1. Molecular association in two-dimension (2D) vs. three-dimension (3D) in cellular signaling. (*A*) Simplified schematic of a RTK signaling pathway. The growth factor brings about dimerization, activation, and intracellular autophosphorylation of the RTK, which recruits cytosolic proteins to the membrane. Sos, a key GEF protein for Ras GTPase activation, is recruited to the cell membrane via the adaptor protein Grb2. Membrane-associated Sos activates Ras, which activates the MAPK cascade. (*B*) Schematic of association in 3D in the cytosol vs. 2D on a membrane. (*C*) Our approach to directly compare rates in 2D vs. 3D: a controllable DNA association reaction monitored on supported membranes, and in buffers with or without viscogens.

quantitation under controlled conditions: buffer solutions supplemented with crowding agents/viscogens to mimic the 3D physical environment of the cytoplasm and supported phospholipid bilayers to represent 2D cell membranes (Fig. 1*C*). Each of these systems has a long history of generating mechanistic insights into biological processes occurring in cellular environments (4, 25, 26). Supported membranes preserve the hallmark lateral fluidity of cell membranes, with diffusion largely determined by the viscosity of the lipids. Dynamics in buffer solutions can be further benchmarked with undiluted cytosolic extracts, which retain the composition and concentrations of cytosolic molecules. Direct comparison of association on the membrane versus in the cytoplasm unequivocally shows that, under conditions relevant to cellular signaling, association at the membrane is faster than in solution. Detailed kinetic analysis revealed that efficient 2D searches are partly attributable to a faster encounter rate at the membrane, with additional effects originating from slow dissociation and orientation effects. This type of rate enhancement is expected to be especially consequential for membrane-associated enzymes that are highly processive; this applies to the seminal example of Ras activation by SOS.

Results

Measuring the Association Rates of an Identical Reaction in Solution and on Membranes. The association reaction we chose to study was the association of protein-sized complementary DNA strands to each other (Fig. 1*C*). By coupling a fluorescent dye to one strand and a fluorescent quencher to its complement, association can be monitored as fluorescence decay in real time (Fig. 1*C* and *SI Appendix*, Fig. S1 *A*–*C*) (27). Because short DNAs are relatively predictable in terms of structure, thermodynamics, and kinetics (27–29), they are particularly useful for elucidating the dynamical effects of membrane localization. DNA association reactions are also robust and relatively easy to control. In addition, the slow dissociation rates of double-stranded DNA allow association rates to be determined directly, simplifying the analysis. In the following experiments, we monitored association reactions over timescales of $\lesssim 10^3$ s, whereas the average lifetime of the DNA complexes used was $\gtrsim 10^6$ s (*SI Appendix*, Fig. S1*D*). Although DNA strands differ from proteins in terms of their flexibility and charge, the experimental advantages of the system make it a good choice for these first experiments directly comparing membrane and cytoplasmic association reactions.

The use of DNA enables us to initiate the association reaction through strand-displacement reactions, thereby defining the zero timepoint of the reaction (27–29). Measuring association rates on membranes is potentially problematic because the DNA strands could associate during the coupling of the fluorescent (F) and quencher (Q) strands to membrane lipids. To prevent this, strands were protected with complementary DNAs: a blocker strand (B) for the fluorescent strand, and a quencher anchor (A) for the quencher strand (Fig. 2*A*), using DNA sequences adapted from previous work on lipid–lipid encounters (27) (*SI Appendix*, Fig. S1*A*). The F and A strands were functionalized with sulfhydryl groups to allow them to be covalently coupled to maleimide-derivatized lipids (30). The association reaction of interest, F to Q, was then initiated by the addition of an initiator strand (I) with a higher affinity for the blocker (B) than the blocker had for the fluorescent strand (F). The initiator binds to the toehold region on B and then outcompetes F in a strand displacement process. F is then free to diffuse and bind to its complementary strand Q through a second toehold-mediated strand displacement process. Blocking was found to protect about 80% of strands and the protection remained stable over hours. Although strand-displacement reactions are not necessary to time-resolve reactions in solutions, we followed this identical protocol for consistency.

Using this approach, we determined the rate constants for association in solution and at the membrane by titration experiments (Fig. 2 *B*–*E*). For the solution reactions (Fig. 2 *B*–*D* and *SI Appendix*, Fig. S1), fluorescence was measured in a fluorometer; for the membrane experiments (Fig. 2*E*), we used epifluorescence microscopy. To generate a family of kinetic traces, we varied the concentration of the quencher complex [Q:A] between 0 and 100% of the fixed total concentration of [B:F]. As a control, we measured the photobleaching rate in the absence of the quencher complex (Q:A), which accounted for less than 5% of total molecules (*SI Appendix*, Fig. S1*F*); thus, most of the fluorescent decay was due to quencher–fluorophore association. Because the reaction consists of two sequential strand-displacement reactions (I displacing B and F displacing Q), we simplified the reaction kinetics by conducting these experiments with an excess of the initiator strand (I) as compared with the fluorescent complex (B:F). Under these conditions, the first strand displacement reaction could be regarded as essentially instantaneous, and the rate-liming step was the association of the fluorescent strand (F) with the quencher (Q) (*SI Appendix*, Fig. S1*E*) (27). In the simplest case, the association can be described by a bimolecular reaction mechanism:

$$F + Q \xrightarrow{k} F{:}Q, \qquad [1]$$

and the kinetics is given by

$$\frac{dF{:}Q(t)}{dt} = kF(t)Q(t) = k\left[F_{tot} - F{:}Q(t)\right]\left[Q_{tot} - F{:}Q(t)\right], \qquad [2]$$

where $F{:}Q(t)$ is the concentration of the $F{:}Q$ complex, $F(t)$ is the concentration of uncomplexed fluorescent strands, F_{tot} is the total concentration of fluorescent strands, $Q(t)$ is the concentration of free quencher strands, Q_{tot} is the total concentration of quencher strands, and k is the bimolecular association rate constant. Note that the units of k are concentration^{-1} time^{-1} for 3D

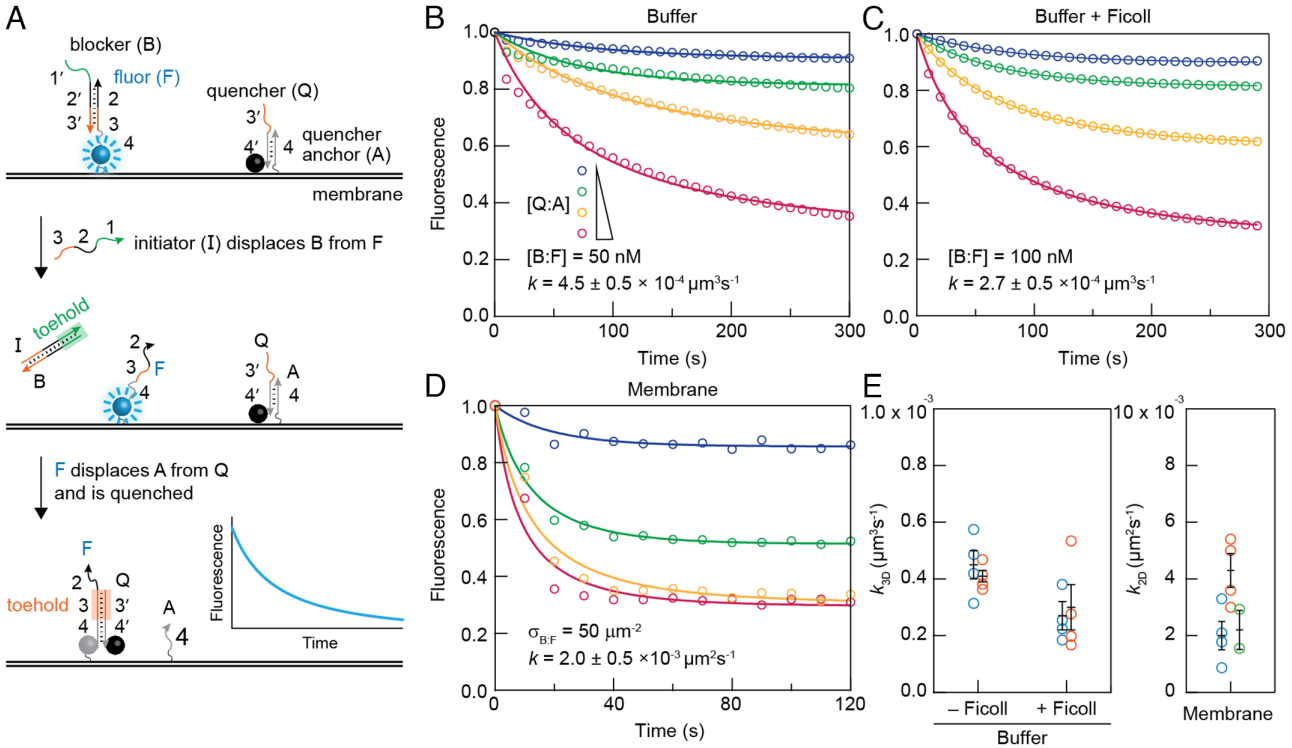

Fig. 2. Association reactions in solution and on membranes. (*A*) Schematic view of the strand displacement reaction. (*B–D*) Normalized traces of fluorescence as a function of time after initiating the DNA strand-displacement reactions in (*B*) phosphate-buffered saline, (*C*) phosphate-buffered saline plus 10% (w/w) Ficoll 70, and (*D*) on supported membranes. In these titration experiments, the fluorescent complex (B:F) was fixed; the quencher complex (Q:A) in solution titration was {50, 25, 10, 5} and {100, 50, 25, 10} for *B* and *C*, respectively; for membrane experiments, the quencher was incubated at {1×, 0.75×, 0.5×, 0.25×} of the fluorescent complex during the coupling reaction. The fitted *Q*s were {36, 19, 8.1, 4.2} nM, {63, 39, 22, 12} nM, and {28, 31, 25, 9.1} molecules/μm^2 for *B–D*, respectively. Membrane data shown here have been corrected for photobleaching (*SI Appendix*, Fig. S5). Solid curves are fits of Eq. **3**. The rate constants are averages ± SEM with $n = 4$. (*E*) Statistics from independent replicates of experiments in *B–D*. A second set of experiments is shown in *SI Appendix*, Fig. S6.

solution experiments and surface density^{-1} time^{-1} for 2D membrane experiments. This equation can be solved in closed form (*SI Appendix*), with the time course of fluorescence given by

$$\frac{F(t)}{F_{tot}} = \frac{1 - \frac{Q_{tot}}{F_{tot}}}{1 - \frac{Q_{tot}}{F_{tot}} e^{-(F_{tot} - Q_{tot})kt}}. \quad [3]$$

Q_{tot} and k were inferred by nonlinear curve fitting. For supported membrane experiments, F_{tot} was measured by fluorescence correlation spectroscopy (FCS) to account for the coupling efficiency (*SI Appendix*, Fig. S2). The solution experiments did not involve covalent coupling reactions, so F_{tot} was directly known. In a later section, we extend this treatment to a more realistic two-step model; nevertheless, under the experimental conditions, the time course of the two-step model is well-approximated by Eq. **3**.

For buffer without Ficoll, fitting Eq. **3** to the data yielded a rate constant k of 2.6 ± 0.2 × 10^5 M^{-1} s^{-1} (mean ± SEM, unless stated otherwise; $n = 8$; see the statistics method in *SI Appendix*), or 4.3 ± 0.3 × 10^{-4} molecules^{-1} μm^3 s^{-1} (Fig. 2 *B* and *E*). In buffer plus the viscogen Ficoll 70 at a concentration (10% w/w) that yielded diffusion constants similar to those seen in organelle-containing cytoplasm (31) (see below), the data yielded a rate constant k of 1.7 ± 0.2 × 10^5 M^{-1} s^{-1}, or 2.8 ± 0.4 × 10^{-4} molecules^{-1} μm^3 s^{-1} (Fig. 2 *C* and *E*; $n = 8$), which is about half of that in buffer without Ficoll.

Next, we measured the association rate on supported membranes (Fig. 2*D*). The membranes consisted of fluid dioleoylphosphatidylcholine (DOPC) bilayers containing 5% maleimide-derivatized dioleoylphosphatidylethanolamine (DOPE), prepared from sonicated unilamellar vesicles (*SI Appendix*). We then used thiol-maleimide crosslinking to couple DNA strands to the derivatized DOPE and anchor them in the membrane (30). *SI Appendix*, Fig. S3 shows the DNAs attached to the bilayers were mostly mobile. We were able to generate a wide range of DNA densities on membranes by this method, from tens to hundreds of molecules per μm^2, as quantified by FCS (*SI Appendix*, Fig. S2). After density determination, strand-displacement reactions were initiated and followed by epifluorescence microscopy. Strand-displacement reactions were verified to be functional on supported membranes by checking that the fluorescence decay was dependent on quenchers (Q) and initiators (I) (*SI Appendix*, Fig. S4). For these experiments, photobleaching was non-negligible (~25%), so data were corrected for photobleaching prior to fitting (*SI Appendix*, Fig. S5). We found the reaction to be remarkably fast on membranes (<100 s for ~100 molecules μm^{-2}); therefore, most of our experiments focused on lower DNA densities (<100 μm^{-2}). Titration with a series of Q:A concentrations yielded a rate constant k of 2.8 ± 0.7 × 10^{-3} molecules^{-1} μm^2 s^{-1} ($n = 3$) (Fig. 2*E*).

We confirmed that DNA molecules (F:B complexes) diffused more slowly on supported membranes than in buffer, buffer plus Ficoll, and cytosolic extracts using FCS (Fig. 3*A*). In all cases, a simple diffusion model fit the FCS autocorrelation data satisfactorily, without the need to invoke anomalous diffusion. The membrane diffusion coefficient (D) was 3.0 ± 0.6 μm^2 s^{-1} (95% CI), which is typical of a molecule anchored to a fluid lipid in supported membranes (32, 33). In solution, the diffusion coefficients were higher: 39.6 ± 1.6 μm^2 s^{-1} in buffer without Ficoll 70; 14.1 ± 2.1 μm^2 s^{-1} (95% CI) in buffer plus Ficoll; and 21.2 ± 3.1 μm^2 s^{-1} in cytosolic extract. We also compared the diffusion of DNA complexes to the 68 kDa protein bovine serum albumin (BSA) (Fig. 2 *B–D*). In buffer ± Ficoll, diffusion coefficients for DNA and BSA

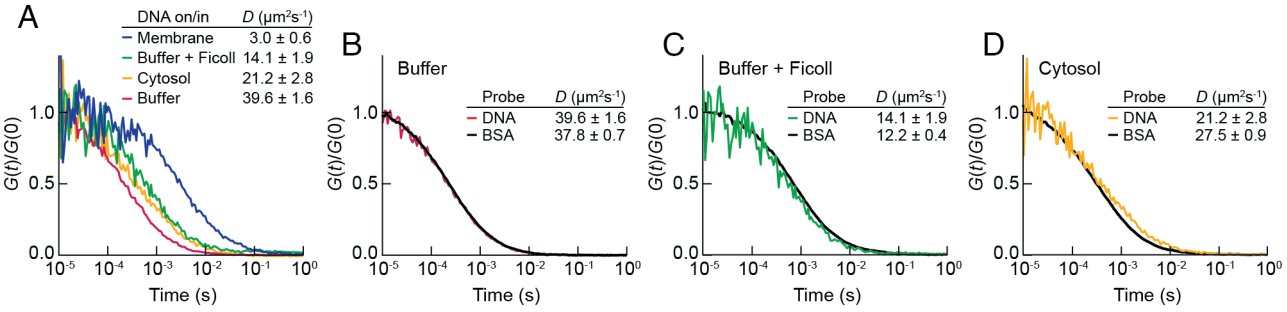

Fig. 3. Diffusion characterization in solution and on membranes. (*A*) Normalized FCS autocorrelation functions of DNA F:B complexes. Diffusion coefficients were obtained from fitting a 3D Brownian model to the data, except in the case of membranes, in which a 2D Brownian model was used. Diffusion coefficients are shown as fitted values ± 95% CI fitting. (*B–D*) Normalized FCS autocorrelation functions for DNA F:B complexes to BSA-Alexa Flour 488 (black) in (*B*) buffer, (*C*) buffer plus 10% Ficoll 70, and (*D*) cytosolic *Xenopus* egg extracts.

were very similar, suggesting that the DNA construct has a similar length scale (we estimate that the DNA has a long axis of about 11 to 13 nm; BSA has a long axis of about 14 nm, and based on its partial crystal structure, Sos has a long axis of at least 13 nm, PDB: 3KSY). The diffusion coefficients in 10% Ficoll 70 were close to those for protein probes in cytoplasmic *Xenopus* egg extracts, which contain organelles in addition to cytosolic components (31). Diffusion of DNA in cytosol was slightly slower than expected from the behavior of BSA, possibly because of partial binding to cytosolic proteins. Although diffusion in both membranes and solutions was slightly faster than typical values observed in cells (D ~1 $\mu m^2\ s^{-1}$ and ~10 $\mu m^2\ s^{-1}$, respectively) (26, 34), the buffer, buffer plus Ficoll, and supported membrane model systems were reasonable approximations of diffusion in cells both in terms of the absolute magnitude of the diffusion coefficients and the fold-differences between solutions and membranes.

Association Is Faster at the Membrane than in Solution. Given that diffusion was 5- to 13-fold slower on membranes than in 3D solutions, we asked whether the association reaction was faster or slower. The rate constants from solutions and membranes cannot be directly compared because of their different units; we therefore calculated total reaction rates. In solution, the reaction rate is given by $k_{3D}c_1c_2$, where k_{3D} is the 3D rate constant in molecules^{-1} μm^3 s^{-1}, and c_1 and c_2 are the concentrations of the fluor and the quencher in molecules μm^{-3}. Units for the total reaction rate are molecules μm^{-3} s^{-1}, so the total number of complexes formed per unit time in a hypothetical cell with a volume V is $k_{3D}c_1c_2V$. Likewise, the reaction rate at the membrane is $k_{2D}\sigma_1\sigma_2$, where k_{2D} is the 2D rate constant in molecules^{-1} μm^2 s^{-1} and σ_1 and σ_2 represent the surface densities of the fluor and quencher in molecules μm^{-2}. Thus, the total reaction rate for a hypothetical cell with a surface area A is $k_{2D}\sigma_1\sigma_2A$. We then define a dimensionless metric R, the rate enhancement factor after translocation to the membrane, as the ratio between total reaction rates at the membrane and in solution:

$$R \equiv \frac{k_{2D}\sigma_1\sigma_2 A}{k_{3D}c_1c_2V}. \quad [4]$$

If $R < 1$, association in 2D at the membrane is faster than association in 3D in the cytosol; if $R < 1$, cytosolic association is faster.

If we assume equal total numbers of associating molecules N_1 and N_2 in the 2D case and the 3D case (Fig. 4*A*), then $\sigma_i = N_i/A$ and $c_i = N_i/V$. For a roughly spherical hypothetical cell, Eq. **4** becomes

$$R_N = \frac{k_{2D}N_1N_2V}{k_{3D}N_1N_2A} \approx \frac{k_{2D}\frac{4}{3}\pi r^3}{k_{3D}4\pi r^2} = \frac{k_{2D}}{k_{3D}}\frac{r}{3}, \quad [5]$$

where the subscript N in R_N reminds us of the assumption of equal numbers of molecules. Note that the volume-to-area ratio, which determines the degree of condensation from 3D to 2D, is maximal for a sphere; other geometries can be accounted for by using the appropriate volume-to-area ratio (*SI Appendix*, Fig. S7).

Eq. **5** shows that the ratio R_N depends upon the size of the cell (Fig. 4*B*). For a 10-μm-radius spherical cell (4 pL in volume; roughly the volume of a mammalian hepatocyte), association would be 22-times faster (±6) if we used the rate constants for membranes (Fig. 2*E*) vs. buffer without Ficoll (Fig. 2*B*) and 33-times faster (±10) for membranes vs. buffer plus 10% Ficoll (Fig. 2*C*). For a 3-μm-radius budding yeast, R_N is 6.5 to 10, and for a 600 μm radius *Xenopus* egg, it would be 1,300 to 2,000. For a 1-μm-radius spherical bacterium, there would be little advantage (R_N = 2 to 3) of 2D association over 3D (Fig. 4*B*). These findings suggest that for most eukaryotic cells, membrane localization substantially promotes intermolecular association and for many prokaryotic cells it does not.

It has been argued that the advantage of membrane localization is that the protein and its target are closer than they would be in 3D. This idea can be tested by comparing 2D vs. 3D reactions in the condition where the average distance between a molecule and its target is kept constant (Fig. 4*C*). We used a statistical approach to derive the nearest-neighbor distance distribution $w(x)$ for random non-interacting particles in 3D (35) and 2D (Fig. 4*D*; derivation shown in *SI Appendix*). In 3D, the mean distance $\langle x_{3D}\rangle \approx 0.554c^{-1/3}$, and in 2D, $\langle x_{2D}\rangle = 0.5\sigma^{-1/2}$, where c is target's concentration in units of molecules μm^{-3} and σ is in molecules μm^{-2}. If we set the values of N_2 on the membrane and in the cytosol so as to satisfy the relationship $\sigma_2 \approx 0.815c_2^{2/3}$ and keep N_1 in the membrane and the cytosol equal, then the mean distances will be the same in the two cases. The ratio of the 2D to 3D rates is then

$$R_d \approx 0.815\frac{k_{2D}\sigma_1c_2^{2/3}A}{k_{3D}c_1c_2V} = 0.815\frac{k_{2D}}{k_{3D}}c_2^{-1/3}. \quad [6]$$

Another method of relating 3D concentration to 2D density is to estimate how many molecules are expected in a plane slicing through a volume filled of evenly distributed molecules. This mapping can be achieved using 1D linear density defined as $\lambda = c^{1/3} = \sigma^{1/2}$ (for example, 1,000 molecules per unit volume on average can be constructed from 10 slabs of 100-molecule planes). The ratio of the 2D to 3D rates at equal linear density is given by

$$R_\lambda = \frac{k_{2D}\sigma_1c_2^{2/3}A}{k_{3D}c_1c_2V} = \frac{k_{2D}}{k_{3D}}c_2^{-1/3}. \quad [7]$$

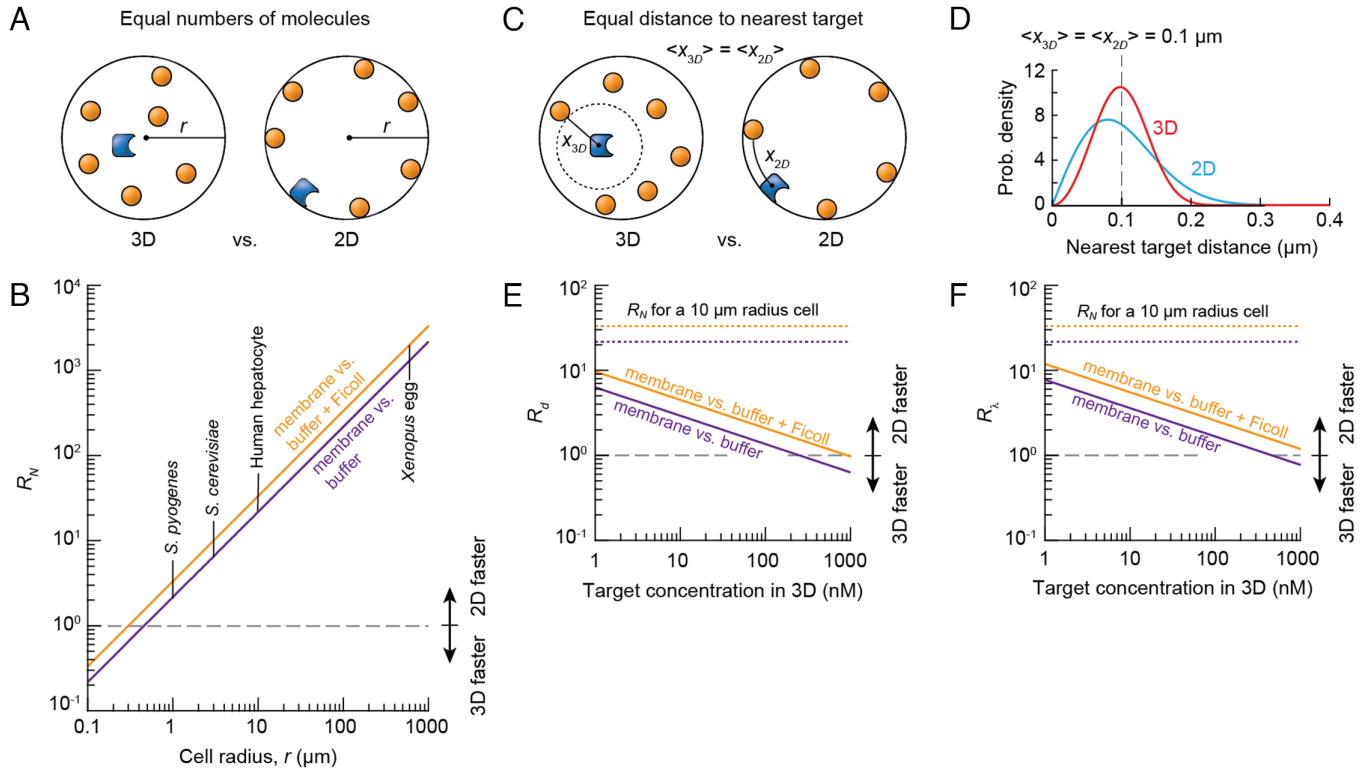

Fig. 4. Association rates in 2D vs. 3D. (*A* and *B*) Changes in association rates when the numbers of molecules are kept constant in 2D and 3D. (*A*) Schematic showing a signaling molecule (blue) and its targets (orange) randomly distributed in the cytoplasm (*Left*) or on the inner aspect of the plasma membrane (*Right*). (*B*) Inferred ratio of the total association rate in 2D divided by the total association rate in 3D (R_N) for spherical cells of various sizes. We assumed equal numbers of molecules in the cytoplasm vs. on the membrane. A value of R_N greater than 1 means that 2D association is faster than 3D association. The diagonal lines are plots of the relationship $R_N = \frac{k_{2D}}{k_{3D}}\frac{r}{3}$ using the value of k_{2D} from the supported bilayer experiment and the value of k_{3D} from either the buffer minus Ficoll (purple) or buffer plus Ficoll (orange) data. The radii of one prokaryote and three eukaryotic cells that span a range of sizes are shown. (*C*–*F*) Changes in association rates while keeping the mean nearest target distance the same in 2D and 3D. (*C*) Schematic showing nearest target distances in 2D and 3D. (*D*) Probability density functions for nearest target distances in 2D (red) and 3D (blue), assuming randomly distributed, non-interacting particles. Concentration (for 3D) and surface density (for 2D) values were chosen so that the average nearest target distance would be 0.1 μm for both cases. (*E*) The ratio of association rates keeping the mean nearest target molecule equal in 2D and 3D, as given by $R_d \approx 0.815\frac{k_{2D}}{k_{3D}}c_2^{-1/3}$. (*F*) The same as *E* except keeping the linear density ($\lambda = c^{1/3}$ for 3D and $\sigma^{1/2}$ for 2D) the same for 2D and 3D.

Note that there is less than a 20% difference between R_d and R_λ.

Eqs. **6** and **7** show that, for target concentrations of less than ~250 nM, 2D association is faster than 3D association even when the mean distance to the nearest target is the same and even though diffusion is an order of magnitude slower (Fig. 4 *E* and *F*). For high-concentration targets, reactions are faster in solution when the distance is identical. Note that many proteins involved in membrane translocation, and their membrane-bound targets, are in fact scarce. For example, Sos is present at a concentration of 2,000 to 12,000 copies per cell in various mammalian cell lines (36), which for an 8.5-μm-radius cell with a volume of 2,600 μm^3 and a surface area of 900 μm^2 corresponds to a concentration of 1.3 to 8 nM, and if the Sos is confined to the membrane, a surface density of 2.2 to 13 molecules μm^2. Thus, for Sos and other scarce signaling molecules, the advantage of membrane localization involves more than just target proximity.

The Rate Enhancement May Arise from a Combination of Efficient 2D Searches, Slowed Dissociation, and Favorable Orientation. Finally, we turned to the issue of how the advantage of 2D over 3D arises; that is, how much of the advantage is due to a change in the encounter rate, and how much is due to other factors. We began by estimating the diffusion-mediated encounter rate, as opposed to the association rate, for the fluorescent and quencher DNA species, to see how much of the enhanced association is due to more frequent collisions. The collision rate cannot be directly measured experimentally, but we can use the Smoluchowski equation to estimate it, given our experimentally measured diffusion coefficients and the sizes of the DNA molecules. In 3D, the collision rate constant $k_{3D} = 4\pi Dd$, where D is the sum of the diffusion coefficients and d is the sum of the molecular radii (14). The value of d is approximately 5 nm for the strand-displacement reactions (27) and the sum of the diffusion coefficients is 79.2 $\mu m^2\ s^{-1}$ in the absence of Ficoll and 28.2 $\mu m^2\ s^{-1}$ in the presence of 10% Ficoll. This yields estimated collision rates of k_{3D} = 3.0 × $10^9\ M^{-1}\ s^{-1}$ or 5.0 $molecules^{-1}\ \mu m^3\ s^{-1}$ in the absence of Ficoll, and 1.1 × 10^9 or 1.8 $molecules^{-1}\ \mu m^3\ s^{-1}$ in the presence of 10% Ficoll. The measured bimolecular rate constants were about 4 orders of magnitude smaller: 4.3 × 10^{-4} $molecules^{-1}\ \mu m^3\ s^{-1}$ for the no-Ficoll case and 2.8 × 10^{-4} $molecules^{-1}\ \mu m^3\ s^{-1}$ in the presence of Ficoll, or ~12,000 and ~6,400 slower, respectively. The calculation is more complicated for collision rates in 2D; the rate constants are time-dependent, with $k_{2D} = 4\pi D\left[\ln\frac{4Dt}{d^2} - 2\gamma\right]^{-1}$ where γ is the Euler's constant (18). However, with parameters relevant to signaling and on a timescale of seconds, the diffusion-limited rate constant is approximately constant with respective to time (it decreases by 24% from 1 to 60 s) (20), and $k_{2D} = 5.1$ $molecules^{-1}\ \mu m^2\ s^{-1}$ for $t = 10$ s. Thus in 2D, collisions are about 1,800-fold faster than the measured association rate. Thus, theoretical collision rates are much faster than the measured association rates in both 2D and 3D, indicating that a one-step bimolecular reaction mechanism (Eq. **1**) does not adequately describe the association process. Note

that this is also typical for protein–protein interactions in solution, where association rates are typically ~10^4 to 10^6 M^{-1} s^{-1}, orders of magnitude below the Smoluchowski limit.

This discrepancy can be accommodated by assuming a two-step model (17, 37, 38), where almost all of the collisions are nonproductive and reversible, but a small fraction of collisions lead to essentially irreversible complex formation. This is shown schematically in Eq. **8**:

$$F + Q \underset{k_-}{\overset{k_+}{\rightleftarrows}} F \cdots Q \overset{k_{on}}{\rightarrow} F{:}\,Q, \qquad [8]$$

where k_+ is the diffusion-mediated collision rate constant (either k_{2D} or k_{3D}), k_{on} is the association rate constant, and k_- is the rate constant for escape by diffusion. The failure of most of the encounter complexes, denoted $F \cdots Q$, to go on to form the irreversible species $F{:}\,Q$ could be due to a low probability that the collision complex will be oriented properly (39).

The rate equation for the production and consumption of the encounter complex $F \cdots Q$ in this model is

$$\frac{d[F \cdots Q]}{dt} = k_+[F][Q] - (k_{on} + k_-)[F \cdots Q]. \qquad [9]$$

Given that the collision rate constant k_+ is large (the Smoluchowski limit) and that k_- is orders of magnitude higher than k_{on}, we can make the steady-state assumption: $\frac{d[F \cdots Q]}{dt} = 0$. It follows that $[F \cdots Q] = \frac{k_+}{k_{on}+k_-}[F][Q]$, throughout the time course, which means that the rate of production of the irreversibly quenched complexes is

$$\frac{d[F{:}\,Q]}{dt} = k_{on}[F \cdots Q] = \frac{k_+ k_{on}}{k_{on} + k_-}[F][Q]. \qquad [10]$$

Note that under these assumptions, this two-step mechanism is kinetically equivalent to a one-step bimolecular reaction (Eq. **1**) with an effective forward rate constant of:

$$k_f = \frac{k_+ k_{on}}{k_{on} + k_-}. \qquad [11]$$

k_f has a simple physical intuition if rearranged into:

$$k_f = k_+ P_{on}, \qquad [12]$$

where $P_{on} = \frac{k_{on}}{k_{on}+k_-}$, a quantity between 0 and 1. Eqs. **10**–**12** describe a pair of molecules that collide at a rate determined by k_+ and bind with a probability P_{on} per collision. This expression can be further simplified to $k_f \approx k_+ \frac{k_{on}}{k_-}$ in our case, since $k_- \gg k_{on}$.

Accordingly, we can decompose the consequences of membrane localization into two principal effects: changes in the diffusion-mediated encounter rate and changes in the reaction probability per encounter. Inserting Eq. **12** into Eq. **5** yields:

$$R_N = \left(\frac{k_{+,2D}}{k_{+,3D}}\frac{r}{3}\right)\left(\frac{P_{on,2D}}{P_{on,3D}}\right). \qquad [13]$$

The first parenthetical expression is the advantage of 2D over 3D that arises from changes in the collision rate, which takes into account changes in proximity, search efficiency, and diffusion. It amounts to a net 3.4-fold advantage of when comparing 2D to 3D for a 10-μm spherical cell, given the diffusion coefficients of buffer solution vs. supported membranes; this advantage increases to 9.4-fold when comparing with 10% Ficoll. Thus, the faster collision rate in 2D contributes partly (3.4- to 9.4-fold) to the overall increased association rate (22- to 33-fold) seen experimentally.

The second parenthetical expression in Eq. **13** represents the change in the reaction probability for each encounter. Since overall the experimental value of R_N is 22 to 33 (Fig. 4*B*) and the diffusion-mediated encounter rate account for 3.4 to 9.4, the reaction probability (P_{on}) for 2D is 6.5- to 3.5-fold higher than for 3D (where the first and second numbers are again referencing to buffers without and with Ficoll, respectively). This result argues that the increased reaction probability is similar in importance to the increased collision rate for promoting association on the membrane.

We can break down the change in reaction probability further. We can estimate k_-'s contributions to P_{on} ($P_{on} \approx k_{on}/k_-$) by calculating the rate at which two molecules in an encounter complex diffuse a critical distance apart (x) (38). Assuming this critical distance to be twice the reaction radius for both solution and membrane cases (38), $k_{-,3D} = \frac{3D}{d^2} = 9.5 \times 10^6$ s^{-1} for buffer solution, $k_{-,3D} = 3.4 \times 10^6$ s^{-1} for Ficoll solution, and $k_{-,2D} = \left(\frac{x^2-d^2}{4D} + \frac{d^2 \ln(d/x)}{2D}\right)^{-1} = 0.6 \times 10^6 s^{-1}$; thus, the retention time of the encounter complex is 16- to 5.6-fold longer on membranes. Given that P_{on} increases by only 6.5- to 3.5-fold on membranes, k_{on} apparently decreases by 2.5- to 1.6-fold. Therefore, this estimate suggests that both the escape rate and association rate decrease at the membrane, but the escape rate's decrease is substantially greater, leading to an increased reaction probability per encounter at the membrane.

One of the various factors that might influence k_{on} is the likelihood that the encounter complex will be oriented properly to allow successful association. A priori it would seem that in 3D, where there are three degrees of rotational freedom, there would be a much higher proportion of unsuccessful orientations than there would be in 2D, where there is only one axis of rotation. This led us to test whether or not the likelihood of a permissive orientation impacts the association rate. To this end, we examined the association of DNA strands in 2D and 3D using an inverted quencher strand with the thiol coupling site moved to the other end of the DNA molecule (Fig. 5*A*). The expectation was that association in 2D would be more affected than in 3D because the restriction in two-dimensional orientation makes proper alignment less probable for the inverted configuration, resulting in a decrease in R_N. Note that the inverted strands can still bind by zippering parallel (instead of perpendicular) to the membrane surface. The efficiency of such an orientation has also been demonstrated in previous studies of the association of DNA strands residing in different apposed lipid bilayers (40).

Solution measurements showed that inverting the DNA strand decreased its association rate constant by a factor of 2.5, presumably due to a short overhanging linker sequence at the toehold region. In comparison, the association rate on membranes decreased by a factor of 6.8. Hence, the advantage of membrane localization decreased by 2.7-fold though it remained more favorable ($R_N = 6.5r/3$ vs. $R_{N,i} = 2.4r/3$; Fig. 5 *B* and *C*). This result confirms that the physical constraint on orientation provided by membrane localization matters for this reaction, although the magnitude of the orientation effect is modest.

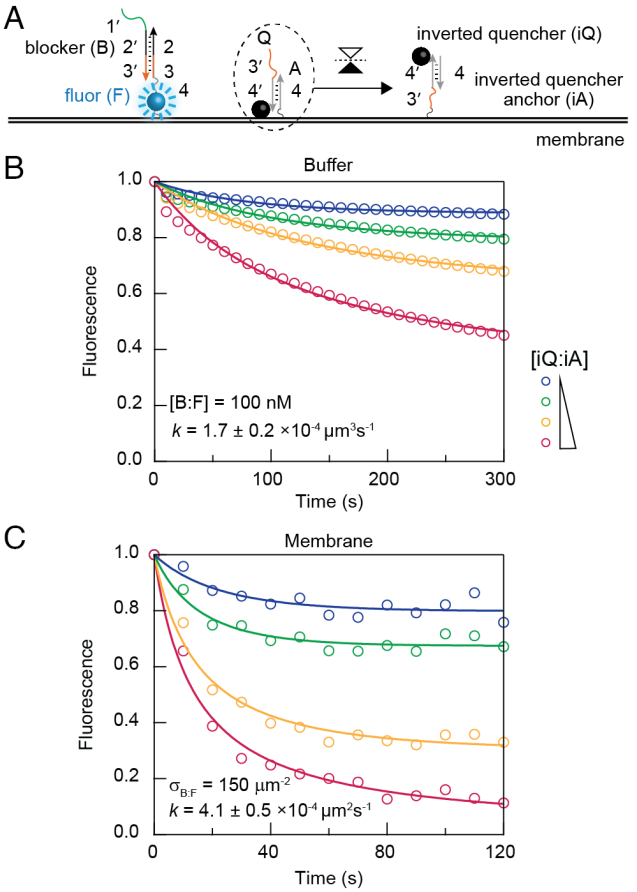

Fig. 5. Inverting quencher orientation affects membrane advantage. (*A*) Schematic view of the binding of a fluorophore-containing strand to an inverted quencher on supported membranes. When coupled to the supported membrane, the iQ:iA strand has an inverted orientation compared to the B:F and Q:A strand. This orientation was achieved by moving the thiol coupling site from the end of the A strand to the Q strand. (*B* and *C*) Titration experiments of the inverted DNA reaction in (*B*) buffer and (*C*) on membranes. The titrated iQ:iA concentration and density were {100, 50, 25, 10} nM and {1×, 0.75×, 0.5×, 0.25×} for *B* and *C*, respectively.

Discussion

In summary, from measurements of association rate constants for complementary DNA strands whose diffusion dynamics are comparable to those of a typical monomeric protein (BSA), we found that association is generally faster when the strands are anchored to a fluid-supported membrane bilayer than when they are free in solution. This study presents direct experimental evidence on this longstanding question. For a 10 μm spherical cell, the increase in association rate would be 22- to 33-fold. The magnitude of the effect depends upon the size of the cell; for most eukaryotic cells, the effect should be substantial, whereas for most prokaryotic cells, it should be minimal. Note that regulated translocation to the membrane appears to be commonplace in mammalian cells, and at least one example is known in budding yeast—the translocation of Ste5 between the plasma membrane and the cytoplasm (41–44). However, we do not know of an example of regulated membrane localization and 2D searches in prokaryotes.

As previously hypothesized, some of the advantage of 2D over 3D can be attributed to an increase in the encounter rate, which arises from increased proximity and the greater efficiency of a 2D search. These findings provide empirical support for the original proposal of Adam and Delbrück (13). In addition, there is an increase in the reaction probability per encounter, and it is comparable to the increased encounter rate. Multiple positive and negative factors may contribute to the overall reaction probability. One is the orientation effect; the loss of two degrees of rotational freedom should dramatically alter the conformational ensemble. Studies with flipped quencher strands did provide evidence for an orientation effect, although the magnitude of the effect was modest. Note that slower diffusion in the viscous membrane environment means that molecules spend more time in the encounter complex, thereby giving them more opportunity to align, which could figure into the relative rates of association vs. dissociation. One caveat here is that although the translational diffusion of the DNA strands being studied here is very similar to that of a BSA-sized protein (Fig. 3), other dynamical properties could be different, and these differences could be critical for the orientation effect.

Some proteins diffusing in cell membranes may have slower diffusion rates (34) than those seen here. This would be expected to decrease the 2D encounter rate but possibly increase the reaction probability (Eq. **13**). Furthermore, note that in the current experiment, the membrane is homogeneous. This is not necessarily the case in cells, where restriction of the binding partners to particular regions within the membrane through lateral phase separation or other types of organization could further increase the advantage of 2D over 3D (45–47).

One final question is how the advantage of 2D over 3D would apply to the particular signaling process we started with, the activation of Ras by Sos. If Ras and Sos were both cytoplasmic, there would be only one search involved in the activation of Ras by Sos, a 3D random walk. However, with Ras being constitutively membrane bound, Sos must first find a (scarce) activated RTK and only then perform a 2D random walk to find Ras. A single 3D random walk has been replaced by a 3D random walk plus a 2D random walk. However, Sos is highly processive on membranes: a single activated Sos molecule at the membrane can activate hundreds of Ras molecules before it dissociates (5, 9). Thus, the activation of multiple Ras molecules by membrane-localized Sos instead of cytoplasmic Sos replaces perhaps hundreds of slow 3D searches with one 3D search followed by hundreds of efficient 2D searches. In general, the greater the magnitude amplification generated by a signaling reaction, the greater the advantage of membrane localization.

Note that reduction of dimensionality is implemented differently here than in it is in the interaction of transcription factors with DNA, one of the processes that motivated Adam and Delbrück. In what is now sometimes termed the standard model for the binding of transcription factors to specific enhancer sites on DNA, a combination of 3D searches for a nonspecific DNA strand followed by 1D searches for the enhancer speeds up the target-finding process (48). For membrane-associated proteins, processivity means that there are repeated applications of reduction of dimensionality for each of many target searches, thereby amplifying what may otherwise be a weaker 3D-to-2D effect compared to that of 3D-to-1D. Nevertheless, the conceptual similarity between both cases argues that changes in dimensionality, local concentration, and diffusion coefficients may be trade-offs that evolution has weighed and optimized in a number of different types of biological regulation.

Materials and Methods

DNA Samples. DNA sequences are shown in *SI Appendix*, Fig. S1, based on a previous study (27) with the modification of attaching a thiol group at the 5′ end for membrane tethering (30). All DNAs were synthesized and purified by Integrated DNA Technologies (IDT). DNAs were purchased in a single-stranded form and hybridized according to the protocol suggested by IDT. Before each membrane

experiment, DNAs were reduced by dithiothreitol (DTT) to enable a thiol-maleimide coupling reaction. Details of each step are described in *SI Appendix*.

Solution Measurements. All experiments, including both the solution and membrane version, were performed in standard phosphate buffered saline (PBS) (11.9 mM phosphate, 137 mM NaCl, 2.7 mM KCl, pH 7.4) at room temperature. Buffer mimicking the viscosity of the cytoplasm (49) was prepared with the addition of 10% Ficoll 70 by weight. Fluorescence in solution was measured with a fluorometer (JASCO FP-8300 model). The excitation and emission wavelengths were 496/5 and 524/5 nm, respectively. Data were acquired every 10 s. Additional details are available in *SI Appendix*.

Membrane Measurements. Supported membranes were prepared by depositing small unilamellar vesicles (SUVs) on an acid-treated glass substrate, as detailed in *SI Appendix*. The lipid composition was 5% 18:1 phosphatidylethanolamide-N-[4-(p-maleimidomethyl)cyclohexane-carboxamide] (PE MCC) in DOPC (Avanti Polar Lipids). The DNA density and diffusion on membranes were measured by FCS (50) on an inverted Zeiss LSM 780 scanning confocal microscope. Fluorescence reactions were monitored by epifluorescence on a Nikon TiE inverted microscope. Samples were excited by a 475/28-nm light source that passed through a 474/27-nm bandpass filter and a 493-nm dichroic mirror. Emission signals passed through a 528/38-nm bandpass filter and were collected by an Andor EM-CCD camera (iXon DU-897). Images were acquired every 10 s with an exposure time of 200 ms. To reduce photobleaching, the PBS solution adjacent to supported membranes included 10 mM 2-mercaptoethanol (BME) and 2 mM Trolox. Details regarding all measurements and analyses are described in *SI Appendix*.

Data, Materials, and Software Availability. All study data are included in the article and/or *SI Appendix*.

ACKNOWLEDGMENTS. We thank Youngbin Lim at the Cell Sciences Imaging Facility for microscopy support, Cheng-Ting Tsai for DNA protocols, and Xianrui Cheng and Julia Kamenz for extract protocols. We thank John Kuriyan, Jeremy Thorner, Dan Herschlag, Daniel Fisher, and Asher Spector for insightful discussions. We thank Yuping Chen, Jo-Hsi Huang, and the rest of the Ferrell lab for helpful discussions and comments on the manuscript. This work is supported by the NIH grant 1R35 GM131792 (J.E.F.) and K99 GM143481 (W.Y.C.H.).

1. W. Lim, B. Mayer, T. Pawson, *Cell Signaling* (Garland Science, 2014).
2. J. Schlessinger, Cell signaling by receptor tyrosine kinases. *Cell* **103**, 211–225 (2000).
3. P. Bandaru, Y. Kondo, J. Kuriyan, The interdependent activation of Son-of-Sevenless and Ras. *Cold Spring Harb. Perspect. Med.* **9**, a031534 (2019).
4. J. T. Groves, J. Kuriyan, Molecular mechanisms in signal transduction at the membrane. *Nat. Struct. Mol. Biol.* **17**, 659–665 (2010).
5. W. Y. C. Huang *et al.*, A molecular assembly phase transition and kinetic proofreading modulate Ras activation by SOS. *Science* **363**, 1098–1103 (2019).
6. A. Aronheim *et al.*, Membrane targeting of the nucleotide exchange factor Sos is sufficient for activating the Ras signaling pathway. *Cell* **78**, 949–961 (1994).
7. J. E. Toettcher, O. D. Weiner, W. A. Lim, Using optogenetics to interrogate the dynamic control of signal transmission by the Ras/Erk module. *Cell* **155**, 1422–1434 (2013).
8. J. Gureasko *et al.*, Membrane-dependent signal integration by the Ras activator Son of sevenless. *Nat. Struct. Mol. Biol.* **15**, 452–461 (2008).
9. L. Iversen *et al.*, Molecular kinetics Ras activation by SOS: Allosteric regulation by altered fluctuation dynamics. *Science* **345**, 50–54 (2014).
10. A. J. Marshall, H. Niiro, T. J. Yun, E. A. Clark, Regulation of B-cell activation and differentiation by the phosphatidylinositol 3-kinase and phospholipase Cgamma pathway. *Immunol. Rev.* **176**, 30–46 (2000).
11. B. D. Manning, L. C. Cantley, AKT/PKB signaling: Navigating downstream. *Cell* **129**, 1261–1274 (2007).
12. G. Polya, Uber eine Aufgabe der Wahrscheinlichkeitsrechnung betreffend die Irrfahrt im Strassennetz. *Math. Ann.* **84**, 149–160 (1921).
13. G. Adam, M. Delbruck "Reduction of dimensionality in biological diffusion processes" in *Structural Chemistry and Molecular Biology*, N. D. A. Rich, Ed. (W. H. Freeman & Co., New York, NY, 1968), pp. 198–215.
14. O. G. Berg, P. H. von Hippel, Diffusion-controlled macromolecular interactions. *Annu. Rev. Biophys. Biophys. Chem.* **14**, 131–160 (1985).
15. H. C. Berg, E. M. Purcell, Physics of chemoreception. *Biophys. J.* **20**, 193–219 (1977).
16. D. Axelrod, M. D. Wang, Reduction-of-dimensionality kinetics at reaction-limited cell-surface receptors. *Biophys. J.* **66**, 588–600 (1994).
17. J. M. Haugh, D. A. Lauffenburger, Physical modulation of intracellular signaling processes by locational regulation. *Biophys. J.* **72**, 2014–2031 (1997).
18. D. C. Torney, H. M. McConnell, Diffusion-limited reaction rate theory for two-dimensional systems. *Proc. R. Soc. Lond. A* **387**, 147–170 (1983).
19. B. Mishra, M. E. Johnson, Speed limits of protein assembly with reversible membrane localization. *J. Chem. Phys.* **154**, 194101 (2021).
20. B. N. Kholodenko, J. B. Hoek, H. V. Westerhoff, Why cytoplasmic signalling proteins should be recruited to cell membranes. *Trends Cell Biol.* **10**, 173–178 (2000).
21. M. Schmick, P. I. H. Bastiaens, The interdependence of membrane shape and cellular signal processing. *Cell* **156**, 1132–1138 (2014).
22. T. A. Leonard, M. Loose, S. Martens, The membrane surface as a platform that organizes cellular and biochemical processes. *Dev. Cell* **58**, 1315–1332 (2023).
23. M. A. McCloskey, M. M. Poo, Rates of membrane-associated reactions: Reduction of dimensionality revisited. *J. Cell Biol.* **102**, 88–96 (1986).
24. D. Bray, Signaling complexes: Biophysical constraints on intracellular communication. *Annu. Rev. Biophys. Biomol. Struct.* **27**, 59–75 (1998).
25. R. Gibeaux, R. Heald, The use of cell-free *Xenopus* extracts to investigate cytoplasmic events. *Cold Spring Harb. Protoc.* **2019**, 1–5 (2019).
26. J. A. Dix, A. S. Verkman, Crowding effects on diffusion in solutions and cells. *Annu. Rev. Biophys.* **37**, 247–263 (2008).
27. M. You *et al.*, DNA probes for monitoring dynamic and transient molecular encounters on live cell membranes. *Nat. Nanotechnol.* **12**, 453–459 (2017).
28. D. Y. Zhang, E. Winfree, Control of DNA strand displacement kinetics using toehold exchange. *J. Am. Chem. Soc.* **131**, 17303–17314 (2009).
29. D. Y. Zhang, G. Seelig, Dynamic DNA nanotechnology using strand-displacement reactions. *Nat. Chem.* **3**, 103–113 (2011).
30. M. P. Coyle, Q. Xu, S. Chiang, M. B. Francis, J. T. Groves, DNA-mediated assembly of protein heterodimers on membrane surfaces. *J. Am. Chem. Soc.* **135**, 5012–5016 (2013).
31. W. Y. C. Huang, X. Cheng, J. E. Ferrell Jr., Cytoplasmic organization promotes protein diffusion in *Xenopus* extracts. *Nat. Commun.* **13**, 5599 (2022).
32. J. K. Chung, Y. K. Lee, H. Y. Lam, J. T. Groves, Covalent Ras dimerization on membrane surfaces through photosensitized oxidation. *J. Am. Chem. Soc.* **138**, 1800–1803 (2016).
33. B. P. Ziemba, J. J. Falke, Lateral diffusion of peripheral membrane proteins on supported lipid bilayers is controlled by the additive frictional drags of (1) bound lipids and (2) protein domains penetrating into the bilayer hydrocarbon core. *Chem. Phys. Lipids* **172–173**, 67–77 (2013).
34. M. J. Saxton, K. Jacobson, Single-particle tracking: Applications to membrane dynamics. *Annu. Rev. Biophys. Biomol. Struct.* **26**, 373–399 (1997).
35. S. Chandrasekhar, Stochastic problems in physics and astronomy. *Rev. Modern Phys.* **15**, 1–89 (1943).
36. T. Shi *et al.*, Conservation of protein abundance patterns reveals the regulatory architecture of the EGFR-MAPK pathway. *Sci. Signal.* **9**, rs6 (2016).
37. D. Shoup, A. Szabo, Role of diffusion in ligand binding to macromolecules and cell-bound receptors. *Biophys. J.* **40**, 33–39 (1982).
38. C. DeLisi, The biophysics of ligand-receptor interactions. *Q. Rev. Biophys.* **13**, 201–230 (1980).
39. S. H. Northrup, H. P. Erickson, Kinetics of protein-protein association explained by Brownian dynamics computer simulation. *Proc. Natl. Acad. Sci. U.S.A.* **89**, 3338–3342 (1992).
40. R. J. Rawle, B. van Lengerich, M. Chung, P. M. Bendix, S. G. Boxer, Vesicle fusion observed by content transfer across a tethered lipid bilayer. *Biophys. J.* **101**, L37–39 (2011).
41. S. C. Strickfaden *et al.*, A mechanism for cell-cycle regulation of MAP kinase signaling in a yeast differentiation pathway. *Cell* **128**, 519–531 (2007).
42. M. S. Hasson, D. Blinder, J. Thorner, D. D. Jenness, Mutational activation of the STE5 gene product bypasses the requirement for G protein beta and gamma subunits in the yeast pheromone response pathway. *Mol. Cell. Biol.* **14**, 1054–1065 (1994).
43. C. Sette, C. J. Inouye, S. L. Stroschein, P. J. Iaquinta, J. Thorner, Mutational analysis suggests that activation of the yeast pheromone response mitogen-activated protein kinase pathway involves conformational changes in the Ste5 scaffold protein. *Mol. Biol. Cell* **11**, 4033–4049 (2000).
44. M. J. Winters, R. E. Lamson, H. Nakanishi, A. M. Neiman, P. M. Pryciak, A membrane binding domain in the ste5 scaffold synergizes with gbetagamma binding to control localization and signaling in pheromone response. *Mol. Cell* **20**, 21–32 (2005).
45. L. B. Case, J. A. Ditlev, M. K. Rosen, Regulation of transmembrane signaling by phase separation. *Annu. Rev. Biophys.* **48**, 465–494 (2019).
46. J. K. Chung *et al.*, Coupled membrane lipid miscibility and phosphotyrosine-driven protein condensation phase transitions. *Biophys. J.* **120**, 1257–1265 (2021).
47. S. L. Veatch, S. L. Keller, Separation of liquid phases in giant vesicles of ternary mixtures of phospholipids and cholesterol. *Biophys. J.* **85**, 3074–3083 (2003).
48. S. E. Halford, J. F. Marko, How do site-specific DNA-binding proteins find their targets? *Nucleic Acids Res.* **32**, 3040–3052 (2004).
49. P. Deming, S. Kornbluth, Study of apoptosis in vitro using the *Xenopus* egg extract reconstitution system. *Methods Mol. Biol.* **322**, 379–393 (2006).
50. O. Krichevsky, G. Bonnet, Fluorescence correlation spectroscopy: The technique and its applications. *Rep. Prog. Phys.* **65**, 251–297 (2002).

PNAS

Supporting Information for
Membrane localization accelerates association under conditions relevant to cellular signaling

William Y. C. Huang, Steven G. Boxer, and James E. Ferrell, Jr

Corresponding authors:
Email: wych@stanford.edu (W.Y.C.H.); james.ferrell@stanford.edu (J.E.F.)

This PDF file includes:

Supporting Information Text

Materials and Methods

DNA Preparation. DNA sequences used in this study are shown in Fig. S1. The sequences mostly followed previous work (1), except with the modification of attaching a thiol group for membrane coupling (2). All DNAs were synthesized and purified (HPLC) by Integrated DNA Technologies (IDT). Using secondary structure analysis provided by IDT (OligoAnalyzer), we verified that all sequences used have unfavorable hairpin structures ($\Delta G \gtrsim 0$). All DNAs were ordered in single-stranded form. To prepare complexes (B:F and Q:A), we followed protocols suggested by IDT: an equimolar ratio of single-stranded DNAs were mixed and heated to 94°C for 2 min, and then the sample was then let to anneal back to room temperature over an hour. DNA complexes were then stored in a 4°C freezer.

The thiol-containing DNAs were shipped in an oxidized form, protected by an S=S bond. Thus, a reduction step was needed prior to membrane coupling. We followed recommendations by IDT to reduce the thiol group using dithiothreitol (DTT). Before coupling reactions, 5 μM DNA was mixed with 100 μM DTT (Thermo Scientific) in borate buffered saline (BBS) (10 mM sodium borate, 150 mM NaCl, pH 8.5) (Rockland) at 37°C for an hour. The solution was then desalted using Zeba spin desalting columns (7 kDa molecular weight cut-off; Thermo Scientific) three times. Columns were buffer-exchanged to BBS before use. For consistency, we reduced DNA only before membrane coupling reactions in small batches.

Buffer and Crowding Agent Solutions. All experiments (membranes and solutions) were performed in standard phosphate buffered saline (PBS) (11.9 mM phosphate, 137 mM NaCl, 2.7 mM KCl, pH 7.4) (Fisher Scientific), except for cytosolic extracts. To increase buffer viscosity, we added 10% Ficoll 70 (by weight) (Sigma Aldrich) in PBS buffers. Solutions were stirred overnight to ensure proper mixing.

Cytosolic Extracts. Cytosolic extracts were prepared following the protocol of Deming and Kornbluth (3), except without the energy regeneration mix. To obtain sufficient cytosolic volume, we typically combined two to three fresh batches of eggs. An additional benefit of combining batches of eggs is that the result may be less specific to one batch of eggs. Because of a higher volume than typical extract preparation, we performed a second round of ultracentrifugation for the cytosolic fraction using the same setting as the first round of ultracentrifugation (250,000 g) for 25 min. Final cytosolic extracts were flash-frozen and kept in a -80°C freezer. All Xenopus experiments and animal care followed protocols (APLAC-13307) approved by the Institutional Animal Care and Use Committee (IACUC) of Stanford University. Prior to adding DNA probes, cytosolic extracts were supplemented with 100 μM mirin (Tocris Bioscience) and 20 mM EDTA (Sigma) and incubated for 10 min to inhibit nuclease activities. When adding reagents to solutions (extracts or viscogen agent solutions) for measurements, we minimized dilution by reagents (typically, the solution retained >95% of its concentration, and >90% at the minimum).

Fluorometer. Solution measurements were performed using a JASCO spectrofluorometer (FP-8300 model), which was controlled by the Spectra Manager 2 software. Time course was taken using the Time Course Measurement option in Em Intensity mode. The excitation wavelength was 496 nm (bandwidth 5 nm), and the emission wavelength was 524 nm (bandwidth 5 nm). The response was set to 0.5 s, and the sensitivity was set to medium. Data were typically taken every 10 s. Background fluorescence was always checked prior to measurements. All strand-displacement measurements (solution and membrane) were done at room temperature.
The time-course data were analyzed with a bimolecular reaction: $F + Q \rightarrow F{:}Q$, in which the reaction rate is kFQ, where k is the rate constant, F and Q are the concentrations of the fluorescent and quencher strands, respectively. The integrated rate equation for bimolecular reactions has the form:

$$ln\left(\frac{\frac{Q}{Q_{tot}}}{\frac{F}{F_{tot}}}\right) = (Q_{tot} - F_{tot})kt, \quad \text{Eq. S1}$$

where the subscript tot denotes the total (or initial) concentration of F or Q. Rearranging Eq. S1 gives

$$\frac{Q}{F} = \frac{Q_{tot}}{F_{tot}} \; e^{-(F_{tot}-Q_{tot})kt} = \frac{Q_{tot} - (F_{tot} - F)}{F},$$

$$F = \frac{F_{tot} - Q_{tot}}{\left(1 - \frac{Q_{tot}}{F_{tot}} \; e^{-(F_{tot}-Q_{tot})kt}\right)},$$

$$\frac{F}{F_{tot}} = \frac{\left(1-\frac{Q_{tot}}{F_{tot}}\right)}{\left(1-\frac{Q_{tot}}{F_{tot}} e^{-(F_{tot}-Q_{tot})kt}\right)}. \quad \text{Eq. S2}$$

The last equation of Eq. S2 was used to fit the normalized data. In the fitting procedure, F_{tot} was fixed based on the initial fluorescence intensity, k and Q_{tot} were floating parameters.

Supported Membranes. Small unilamellar vesicles (SUVs) were prepared by mixing 5% (by mol/mol) 18:1PE MCC with DOPC in chloroform, where DOPC stands for 1,2-dioleoyl-sn-glycero-3-phosphocholine and 18:1 PE MCC stands for 1,2-dioleoyl-sn-glycero-3-phosphoethanolamine-N-[4-(p-maleimidomethyl)cyclohexane-carboxamide] (sodium salt) (Avanti Polar Lipids). If visualization of bilayers was required, 0.01% of TR-DHPE was added to the mixture; TR-DHPE stands for Texas Red 1,2-dihexadecanoyl-sn-glycero-3-phosphoethanolamine, triethylammonium salt (Invitrogen). The solution was then evaporated by blowing N_2 for 10 min. Dried lipid films were then resuspended in H_2O by vortexing, resulting in a concentration of 0.5 mg/mL. Finally, vesicle solutions were sonicated for 45 s in an ice-water bath twice to make SUVs. SUVs were stored in a 4°C fridge for experiments on the next day. All experiments used new batches of freshly prepared vesicles for consistency.

Supported lipid bilayers (SLBs) were assembled in a flow chamber system (μ-Slide, Ibidi). Glass substrates were piranha etched (H_2SO_4:H_2O_2 = 3:1 by volume; warning: strong acid) (Fisher Scientific) for 5 min, followed by excessive rinsing with H2O. Substrates were blown dry with air before attaching to the flow chamber system. SLBs were formed on substrates by incubating the prepared SUVs at 0.25 mg/mL mixed in 0.5x tris buffered saline (TBS) (1x TBS: 20 mM Tris, 136 mM NaCl, pH 7.4) for at least 30 min. Chambers were then rinsed with 1x TBS buffers. Next, 1 mg/mL (0.1%) BSA (Sigma) in TBS buffers was incubated for 10 min to block detects in SLBs. Then solutions were exchanged to borate buffered saline (BBS) buffers (10 mM sodium borate, 150 mM NaCl, pH 8.5) (Rockland). Reduced DNAs (see DNA Preparation) were then added to the solution at a desired concentration (~50-200 nM for a typical titration experiment) and incubated for 1 hr (higher densities were achieved with higher concentrations and up to 2.5 hr of incubation). The sample was then heavily washed in the last step with PBS buffers (the imaging condition). All bilayer preparation was done at room temperature, unless stated otherwise.

Fluorescence Correlation Spectroscopy. FCS data were collected with an inverted Zeiss LSM 780 multiphoton laser scanning confocal microscope. Samples were excited by a 488 nm laser line (3 μW) that passed through a 488 beam splitter and focused by a C-APO 40x (FCS-certified) water-based objective. Emissions passed through a variable secondary dichroic (VSD) beam splitter that selected signals from wavelength 499-579 nm. The pinhole was aligned using the Adjust Pinhole function in the software. Signals were collected by the LSM BiG module with GaAsP photodetector, which enabled the selection of detection wavelength. All data were acquired using the ZEN Black software.

The ZEN program calculated time autocorrelation functions by $G_{ZEN}(\tau) = \frac{\langle I(t)I(t+\tau)\rangle}{\langle I(t)\rangle^2}$, where $I(t)$ is the fluorescence intensity, τ is the delay time, and $\langle\cdot\rangle$ denotes the average. This function relates to our definition of autocorrelation function by $G(\tau) = \frac{\langle \delta I(t)\delta I(t+\tau)\rangle}{\langle I(t)\rangle^2} = G_{ZEN}(\tau) - 1$, where $\delta I(t) = I(t) - \langle I(t)\rangle$ (4). Subsequent fitting was performed in Igor Pro (version 6). A Brownian diffusion model was used to fit the autocorrelation data:

$$G_{3D}(\tau) = \frac{1}{N\left(1+\frac{\tau}{\tau_D}\right)\sqrt{\left(1+\frac{1}{s^2}\frac{\tau}{\tau_D}\right)}} \qquad \text{Eq. S3}$$

where N is the particle number, τ_D is the characteristic diffusion time, and s is the structural parameter of the optics and was fixed to 7 as suggested by the manual. For membrane experiments, autocorrelation functions were fitted by a 2D diffusion model: $G_{2D}(\tau) = \frac{1}{N}\left(1 + \frac{\tau}{\tau_D}\right)$. All curve fitting was performed between a time range of 10 μs to 1 s (except spot-size calibrations, where a time range of 1 μs-0.1 s was used). The diffusion coefficient of the sample was calculated by $D = \frac{w^2}{4\tau_D}$, where w is the confocal spot radius and τ_D is the measured diffusion time. The spot-size (w) was calibrated by averaging spot-sizes determined by fluorescein (Sigma Aldrich), Alexa Fluor 488 (Invitrogen), Atto488-carboxylic acid (Atto-Tec), and 0.1 μm TetraSpeck microspheres (Invitrogen) in water at room temperature assuming known diffusion coefficients ($D = 425,435,400$, and 4.4 μm^2/s, respectively). For measurements on supported membranes, it is worth noting that reliable autocorrelation functions and stable intensities are strong indicators of fluid membranes (Fig. S2, 3). We did not see any discernable photobleaching in the intensity traces (even when moving to a new position), suggesting that DNAs were mostly fluid on bilayers. All DNA densities on SLBs were measured independently prior to strand-displacement reactions.

Epifluorescence Microscopy. Monitoring strand-displacement reactions on supported membranes was performed on a Nikon TiE inverted microscope. Samples were excited by a 475/28-nm light source (Lumencor Spectra III) (120 μW). The excitation light passed through a 474/27-nm bandpass filter and a 493-nm dichroic mirror (Sedat quad filter set, Semrock) and focused through a 100x 1.49 N.A. oil immersion objective (Nikon). Emission signals passed through a 528/38-nm bandpass filter (Sedat quad filter set, Semrock) and were collected by an Andor EM-CCD camera (iXon DU-897). Images were acquired every 10 s with an exposure time of 200 ms. All data acquisitions were controlled by the NIS-Elements software. Prior to imaging, the sample was buffer exchanged to PBS buffers containing 10 mM 2-Mercaptoethanol (BME) (Sigma) and 2 mM Trolox (Cayman Chemical) to reduce photobleaching. Strand-displacement reactions were triggered by including initiator strands (I) in the above PBS buffers. Photobleaching was estimated with samples without the initiator strand. Fluorescence intensities from images were extracted in ImageJ. After background subtraction, the intensities were normalized to the initial point. Data were then corrected for photobleaching by dividing each time point by the photobleaching curve. Processed data were then fitted by the same procedure described in the *Fluorometer* section (Eq. S2).

Unit and Unit Conversion. The rate constants k_i derived from solution and membrane experiments were expressed in the unit of M^{-1}s^{-1} and μm^{2}s^{-1}, respectively. The solution rate constants were then converted to the unit of μm^{3}s^{-1} by $M^{-1} = \frac{dm^3}{mole} = \frac{(10^{15}\ \mu m^3)}{6\times10^{23}\ molecule} = 1.67\times10^{-9}\ \frac{\mu m^3}{molecule}$. Thus, $k_{solution} = 2.6\times10^5\ M^{-1}\ s^{-1} = 4.3\times10^{-4}\ \mu m^3 s^{-1}$; $k_{Ficoll} = 1.7\times10^5\ M^{-1}\ s^{-1} = 2.8\times10^{-4}\ \mu m^3\ s^{-1}$. In all subsequent analyses, rate constants have units in μm and s.

Statistics for Fig. 2 titration experiments. To calculate the mean and the standard error of the mean (SEM) of the titration experiments in Fig. 2B-E, we first assessed how the day-to-day variation compared to the measurement error within the same day, then applied the

corresponding formula to calculate the statistics. If the day-to-day variation was smaller or comparable to the measurement error, such as the case in all solution measurements, data points across different days were compiled to calculate the statistics. If the day-to-day variation was larger than the measurement error, such as the case in supported membranes, the average values from different days were compiled to compute the final statistics. All averages were arithmetic averages without weights.

Derivation of distance to the nearest target. In the following, we derive the distance distribution of a single signaling molecule with its nearest target molecule. Particles are randomly distributed and non-interacting. Following the seminal work of S. Chandresekhar (5), we define $w_{3D}(x)$ as the probability of finding the nearest neighbor molecule between x and $x + dx$ in the solution, with the fluorescent molecule marked at the center. By definition:

$$w_{3\mathrm{D}}(x) = \left(1 - \int_0^r \mathrm{w}_{3\mathrm{D}}(x')dx'\right)4\pi x^2 c. \qquad \text{Eq. S4}$$

Note that the concentration adopts a unit of μm^{-3}. Eq. S4 is solved by differentiation and then integration with respect to x:

$$\frac{d}{dx}\frac{w_{3\mathrm{D}}(x)}{4\pi x^2 c} = \frac{d}{dx}\left(1 - \int_0^x w_{3\mathrm{D}}(x')dx'\right) = -w_{3\mathrm{D}}(x) = -4\pi x^2 c\left(\frac{w_{3\mathrm{D}}(x)}{4\pi x^2 c}\right),$$

$$\int \frac{d\left(\frac{w_{3\mathrm{D}}(x)}{4\pi x^2 c}\right)}{\left(\frac{w_{3\mathrm{D}}(x)}{4\pi x^2 c}\right)} = \int -4\pi x^2 c dx,$$

$$\ln\left(\frac{w_{3\mathrm{D}}(x)}{4\pi x^2 c}\right) = -\frac{4}{3}\pi x^3 c, \qquad \text{Eq. S5}$$

from which we obtain:

$$w_{3\mathrm{D}}(x) = 4\pi x^2 c e^{-\frac{4}{3}\pi x^3 c}. \qquad \text{Eq. S6}$$

$w_{3\mathrm{D}}(x)$ describes the full statistical distribution of the nearest target (Fig. 4D). Thus, the average distance is:

$$d = \langle x \rangle = \int_0^\infty r w_{3\mathrm{D}}(r)dr = \Gamma\left(\frac{4}{3}\right)\left(\frac{3}{4\pi c}\right)^{\frac{1}{3}} \approx 0.554 c^{-\frac{1}{3}},$$

$$c = \frac{0.17}{d^3}, \qquad \text{Eq. S7}$$

where Γ is the gamma function.

The nearest-neighbor distribution in 2D is defined similarly:

$$w_{2\mathrm{D}}(x) = \left(1 - \int_0^x w_{2\mathrm{D}}(x')dx'\right)2\pi x\sigma, \qquad \text{Eq. S8}$$

which can be solved following steps in Eq. S5:

$$\frac{d}{dr}\left(\frac{w_{2\mathrm{D}}(x)}{2\pi x\sigma}\right) = \frac{d}{dx}\left(1 - \int_0^x w_{2\mathrm{D}}(x')dx'\right) = -w_{2\mathrm{D}}(x) = -\left(\frac{w_{2\mathrm{D}}(x)}{2\pi x\sigma}\right)2\pi x\sigma,$$

$$\int \frac{d\left(\frac{w_{2D}(x)}{2\pi x\sigma}\right)}{\left(\frac{w_{2D}(x)}{2\pi x\sigma}\right)} = \int -2\pi x\sigma dx,$$

$$\ln\left(\frac{w_{2D}(x)}{2\pi x\sigma}\right) = -\pi x^2\sigma, \qquad \text{Eq. S9}$$

from which we arrive:

$$w_{2D}(x) = 2\pi x\sigma e^{-\pi x^2\sigma}. \qquad \text{Eq. S10}$$

Thus, the average distance in 2D is:

$$d = \langle x\rangle = \int_0^\infty xw(x)dx = \Gamma\left(\frac{3}{2}\right)\left(\frac{1}{\pi\sigma}\right)^{\frac{1}{2}} = 0.5\sigma^{-\frac{1}{2}},$$

$$\sigma = \frac{1}{4d^2}, \qquad \text{Eq. S11}$$

At this point, it is useful to calculate some numbers relevant to cells. An average protein in cells has a concentration of about 200 nM (assuming 1/25,000 of total proteins), which is equivalent to an average distance of about 112 nm; a distance of 100 nm maps to a surface density of about 25 molecules $\cdot$ μm^{-2}.

For a spherical cell of radius r, we can calculate how much the average nearest neighbor distance would change after membrane translocation by using the relationship:

$$\langle x_{2D}\rangle = 0.5\sigma^{-\frac{1}{2}} = 0.5 * \left(\frac{N_2}{A}\right)^{-\frac{1}{2}} = 0.5 * \left(\frac{\frac{4}{3}\pi r^3 c}{4\pi r^2}\right)^{-\frac{1}{2}} = 0.5 * \left(\frac{rc}{3}\right)^{-\frac{1}{2}}. \qquad \text{Eq. S12}$$

If our spherical cell has a radius of 10 μm, then $\langle x_{2D}\rangle \approx 0.274c^{-\frac{1}{2}}$.

Supporting Figures

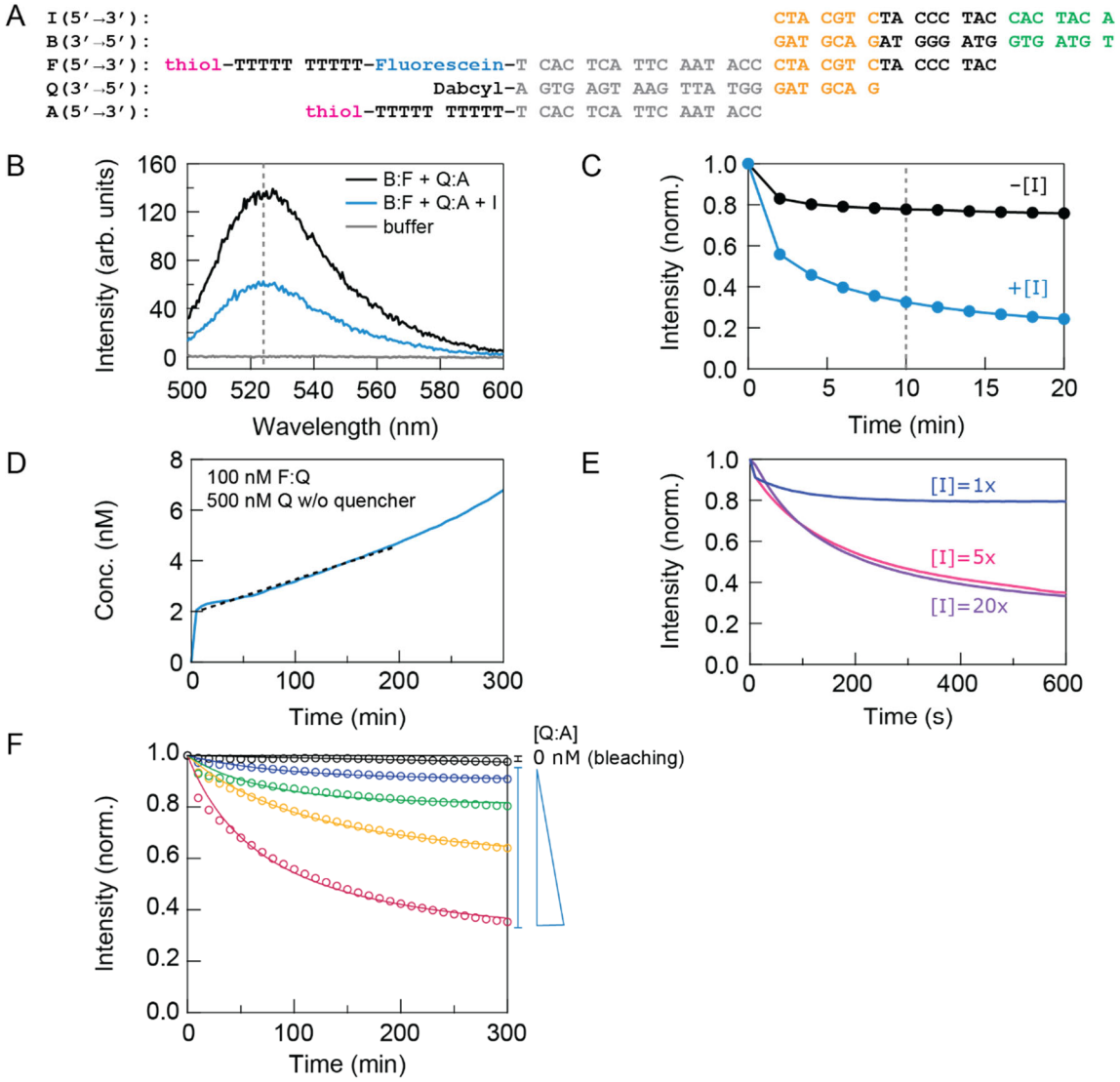

Fig. S1. Characterization of strand-displacement reactions in solution. (*A*) DNA constructs used in this study. The fluorescein derivative used was FAM. When coupled to the membrane, the left side of the sequence was closest to the membrane surface (the thiol group is the coupling site). (*B* and *C*) Fluorescence spectra and time courses of the blocked fluorescent strand (B:F) with and without the initiator strand (I). Dashed lines show the wavelength used to measure the time course (left) and the time point when the spectrum was taken (right). (*D*) Estimation of the upper bound of the dissociation rate of DNA complexes (F:Q). To resolve the dissociated strands, we added complementary strands without the quencher such that most strands, once dissociated, will remain fluorescent. By fitting a linear rate to the early slope (slope $\approx k_{-1}\,[F{:}\,Q]$), the fit yielded a dissociation rate constant of 2×10^{-6} s^{-1}. Note that this estimation is likely higher than the true dissociation rate because the additional complementary strand may compete with the quencher strand (Q). Nevertheless, this slow rate indicates that the average lifetime of these DNA complexes ($\gtrsim 10^6$ s) are much longer than the time course of titration experiments ($\lesssim 10^3$ s) (Fig. 2). Therefore, in these experiments, the number of association events can be approximated by the number of complexes. (*E*) Titration of the initiator strand (I) on the kinetics of strand-displacement reactions. When the initiator's concentration was above 5-fold of the fluorescent strand (F), the kinetics became mostly independent of the initiator's concentration, which

suggests that the rate-limiting step was the fluorescent strand (F) binding to the quencher strand (Q). (*F*) Data in Fig. 2B overlaid with photobleaching control (black) under the same experimental condition. At the end of the experiment, less than 5% of molecules were photobleached.

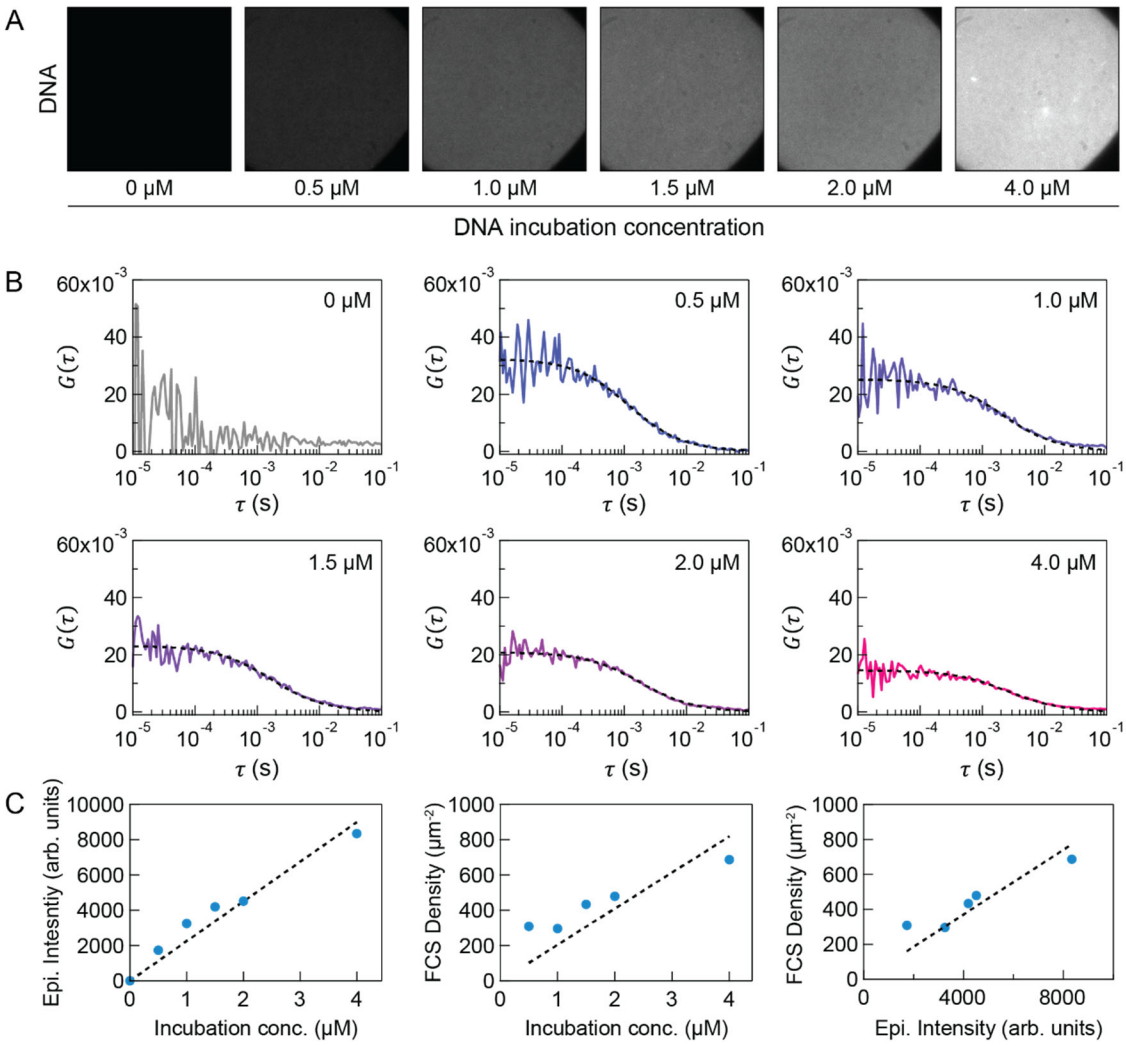

Fig. S2. DNA density titration on supported membranes. (*A*) Epifluorescence images of titrating the fluorescent strand (F) on supported membranes. (*B*) Surface densities of DNA were calibrated by fluorescence correlation spectroscopy (FCS). Dashed lines are fitting of a 2D Brownian model. (*C*) Summary of data shown in *A* and *B*. It was experimentally convenient to have a linear relationship (dashed lines) between surface densities and incubation concentrations, though this linearity was not strictly required for the experiments. We measured the density of all the samples independently prior to strand-displacement reactions.

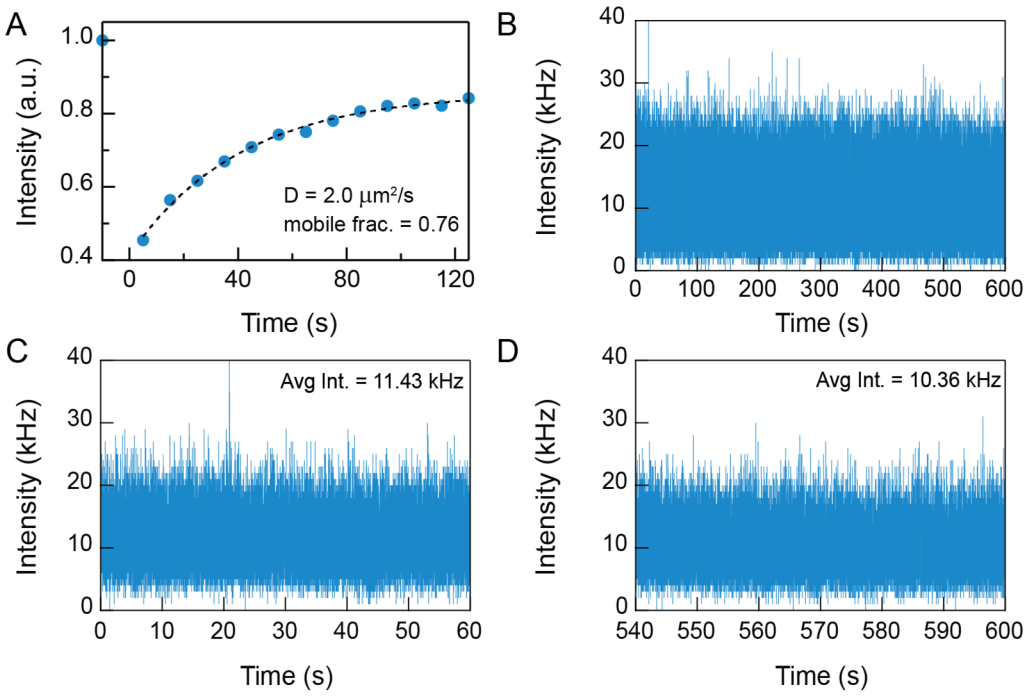

Fig. S3. Fluidity characterization of fluorophore-DNA strands attached to supported membranes. (*A*) Fluorescence recovery after photobleaching (FRAP) of DNA tethered to supported membranes. (*B*) Fluorescence intensity of DNA in a confocal spot of about 200 nm for characterizing local fluidity. (*C, D*) The first and last minute of data in *B*. Note that the final intensity was still about 90% of initial intensity after 10-min of continuous light exposure, suggesting that most of the DNAs were mobile.

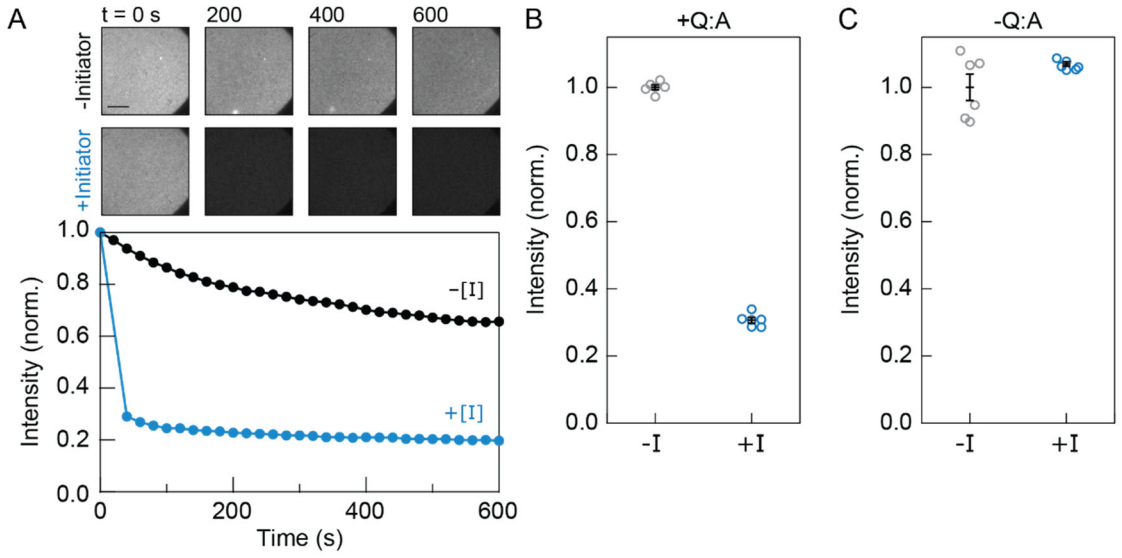

Fig. S4. Characterization of strand-displacement reactions on supported membranes. (*A*) Images (top) and time courses (bottom) of strand-displacement reactions with and without the initiator strand (I) on supported membranes. Note that the initiator-dependent fluorescent decay (blue) was much steeper than the bleaching curve (black) (prior to photobleaching correction). Scale bar, 20 μm. (*B*) Epifluorescence intensities before and after adding initiator at different regions of interest. In contrast to *A*, intensities here were measured without prior exposure to light (i.e., no photobleaching). (*C*) Same as in *B*, except without the quencher strand (Q). Error bars, SEM from 6 different regions of interest (ROI).

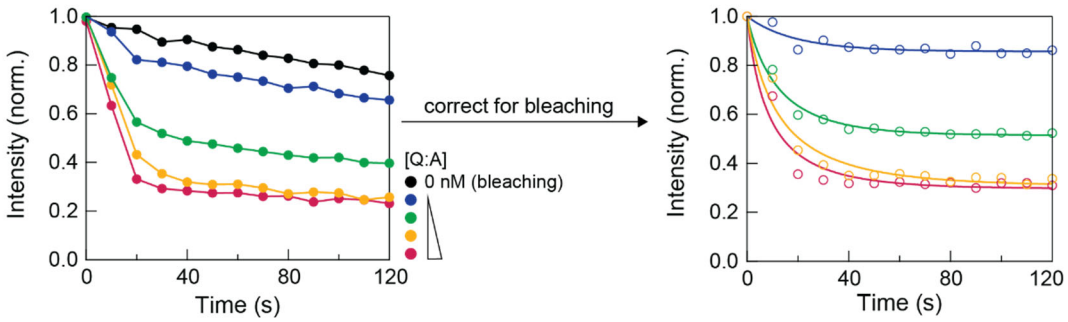

Fig. S5. Photobleaching correction for reactions on supported membranes. Normalized intensity traces before (left) and after (right) photobleaching correction. Data were corrected by dividing the intensity of each time point by that of the bleaching curve (black). Note that, after correction, the kinetic traces plateaued near the end of experiments, suggesting that the correction was appropriate.

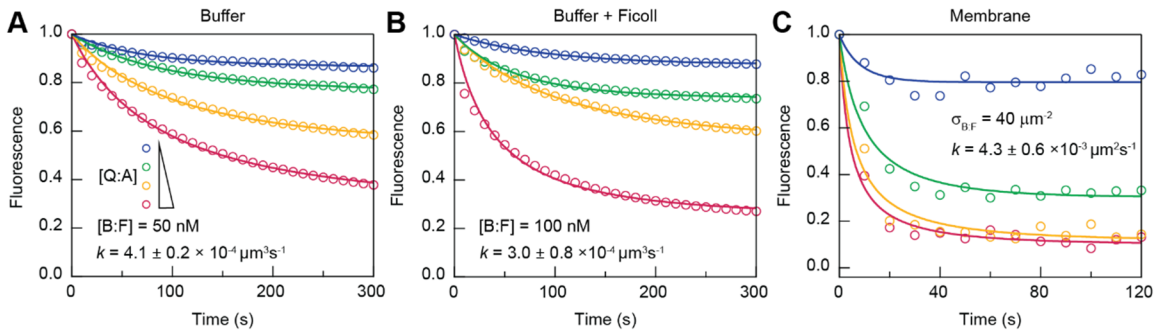

Fig. S6. Association reactions: a set of independent replicates. (*A*-*C*) Independent replicates of experiments shown in Fig. 2B-D (see the figure legend). Statistics are summarized in Fig. 2E.

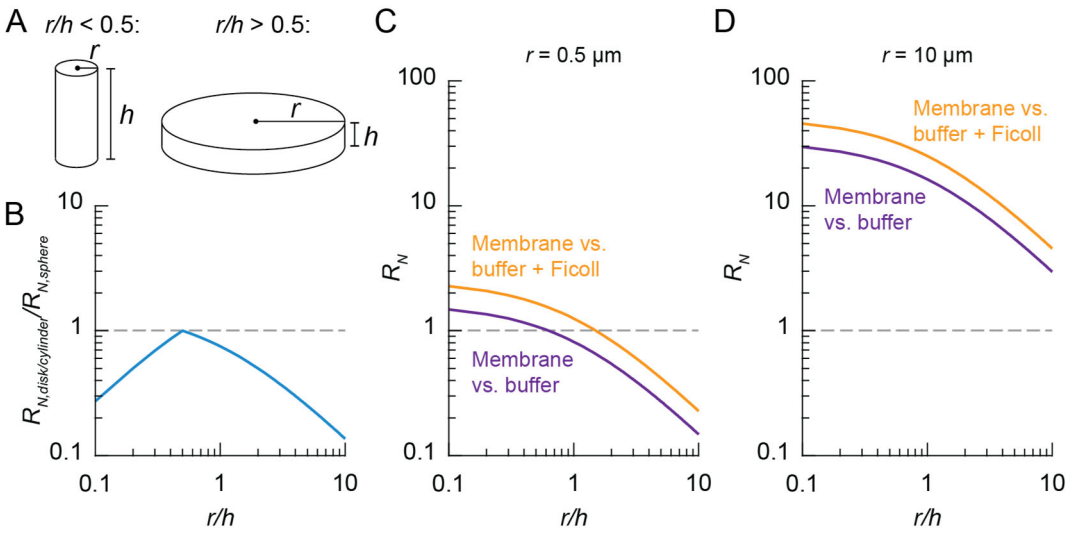

Fig. S7. Other geometry for R_N: cylinders and disks. (*A*) Geometry of a cylinder and a disk. Both shapes are parameterized by the radius and height, with cylinders having $2r < h$ and disks having $2r > h$. In both cases, $\frac{V}{A} = \frac{rh}{2(r+h)}$. (*B*) Comparison of cylinders and disks with spheres. The long axis of a cylinder (h) or disk (2r) is taken as the diameter of the sphere. Thus, for $r/h > 0.5$, $R_N = \frac{k_{2D}}{k_{3D}}\frac{r}{3}\left(\frac{3}{2\left(1+\frac{r}{h}\right)}\right)$; for $r/h < 0.5$, $R_N = \frac{k_{2D}}{k_{3D}}\frac{\frac{h}{2}}{3}\left(\frac{3}{\left(1+\frac{h}{r}\right)}\right)$. The blue curve shows the parenthesis of the R_N expressions. Other shapes relevant to cells have a smaller R_N of about 40-100% of a sphere. (*C* and *D*) R_N of cylinders and disks. For example, a bacterium of $r = 0.5$ μm and $h = 2$ μm gives R_N of 1.3 to 2.0; a mammalian cell of $r = 10$ μm and $h = 5$ μm gives R_N of 11 to 17.

SI References

1. M. You et al., DNA probes for monitoring dynamic and transient molecular encounters on live cell membranes. Nat Nanotechnol 12, 453-459 (2017).
2. M. P. Coyle, Q. Xu, S. Chiang, M. B. Francis, J. T. Groves, DNA-mediated assembly of protein heterodimers on membrane surfaces. J. Am. Chem. Soc. 135, 5012-5016 (2013).
3. P. Deming, S. Kornbluth, Study of apoptosis in vitro using the Xenopus egg extract reconstitution system. Methods in Molecular Biology 322, 379-393 (2006).
4. O. Krichevsky, G. Bonnet, Fluorescence correlation spectroscopy: the technique and its applications. Rep. Prog. Phys. 65, 251-297 (2002).
5. S. Chandrasekhar, Stochastic Problems in Physics and Astronomy. Reviews of Modern Physics 15, 1-89 (1943).